WL-TR-95-2022

ACQUISITION AND REDUCTION OF ROTOR
TIP STATIC PRESSURE TRANSDUCER
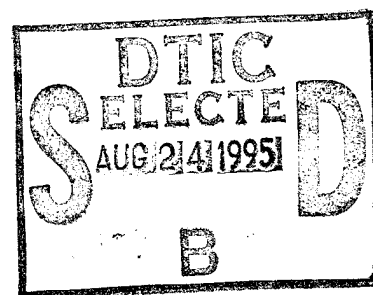DATA FROM A LOW ASPECT RATIO
TRANSONIC FAN

PATRICK M. RUSSLER

BATTELLE MEMORIAL INSTITUTE
APPLIED TECHNICAL COMPUTER GROUP
WRIGHT-PATTERSON AFB   OH   45433-7650

FEBRUARY 1995

FINAL REPORT FOR PERIOD JUNE 1993 TO FEBRUARY 1994

APPROVED FOR PUBLIC RELEASE; DISTRIBUTION UNLIMITED

AERO PROPULSION AND POWER DIRECTORATE
WRIGHT LABORATORY
AIR FORCE MATERIEL COMMAND
WRIGHT-PATTERSON AFB OH 45433-7650

19950822 005

NOTICE

When Government drawings, specifications, or other data are used for any purpose other than in connection with a definitely Government-related procurement, the United States Government incurs no responsibility or any obligation whatsoever. The fact that the government may have formulated or in any way supplied the said drawings, specifications, or other data, is not to be regarded by implication, or otherwise in any manner construed, as licensing the holder, or any other person or corporation; or as conveying any rights or permission to manufacture, use, or sell any patented invention that may in any way be related thereto.

This report is releasable to the National Technical Information Service (NTIS). At NTIS, it will be available to the general public, including foreign nations.

This technical report has been reviewed and is approved for publication.

PATRICK M. RUSSLER
RESEARCH ENGINEER
APPLIED TECHNICAL COMPUTER GROUP
BATTELLE MEMORIAL INSTITUTE

NORMAN D. POTI
CHIEF, TEST & EVALUATION SECTION
TECHNOLOGY BRANCH
TURBINE ENGINE DIVISION
AERO PROPULSION & POWER DIRECTORATE

GEORGE CHARLAN, MAJ, USAF
CHIEF, TECHNOLOGY BRANCH
TURBINE ENGINE DIVISION
AERO PROPULSION & POWER DIRECTORATE

REPORT DOCUMENTATION PAGE

1. AGENCY USE ONLY (Leave blank)	2. REPORT DATE 1995 February	3. REPORT TYPE AND DATES COVERED FINAL JUNE 1993 to FEBRUARY 1994

4. TITLE AND SUBTITLE

Acquisition and Reduction of Rotor-Tip Static Pressure Transducer Data From a Low Aspect Ratio Transonic Fan

6. AUTHOR(S)

Patrick Russler   (513) 255-6802

5. FUNDING NUMBERS

F33615-91-D-2162
PE: 62203F
PR: 3066
TA: 17
WU: 91

7. PERFORMING ORGANIZATION NAME(S) AND ADDRESS(ES)

Applied Technical Computer Group
Battelle Memorial Institute
Wright-Patterson AFB OH 45433-7650

8. PERFORMING ORGANIZATION REPORT NUMBER

9. SPONSORING/MONITORING AGENCY NAME(S) AND ADDRESS(ES)

Aero Propulsion & Power Directorate
Wright Laboratory
Air Force Materiel Command
Wright-Patterson AFB OH 45433-7650

10. SPONSORING/MONITORING AGENCY REPORT NUMBER

WL-TR-95-2022

11. SUPPLEMENTARY NOTES

12a. DISTRIBUTION/AVAILABILITY STATEMENT

APPROVED FOR PUBLIC RELEASE; DISTRIBUTION IS UNLIMITED

12b. DISTRIBUTION CODE

13. ABSTRACT (Maximum 200 words)

This report details the acquisition and reduction of Over-The-Rotor (OTR) static pressure data. These data were acquired during the Augmented Damping of Low Aspect Ratio Fans (ADLARF) test conducted at the Compressor Research Facility (CRF). The CRF is located at Wright Laboratory on Wright-Patterson A.F.B. in Ohio. The CRF is one of two high-speed compressor test facilities at Wright Laboratory.

The report is primarily concerned with the acquisition and reduction of the OTR data, and is intended to demonstrate the ability to reduce, display, and analyze static pressure data acquired from the tip region of fans and compressors. The ability to show basic shock structure in the tip region of a transonic fan is clearly demonstrated. Problems associated with the acquisition and reduction process are also addressed. Although these data were originally intended only to demonstrate proof of concept, they have also provided valuable insight concerning the tip flow region of the ADLARF fan.

14. SUBJECT TERMS

End Wall Flow
Axial Compressor
Aircraft Turbine Engine
Intra-Blade Flow Field
Transonic Fan

15. NUMBER OF PAGES
32

16. PRICE CODE

17. SECURITY CLASSIFICATION OF REPORT	18. SECURITY CLASSIFICATION OF THIS PAGE	19. SECURITY CLASSIFICATION OF ABSTRACT	20. LIMITATION OF ABSTRACT
Unclassified	Unclassified	Unclassified	Unlimited

TABLE OF CONTENTS

LIST OF FIGURES

LIST OF TABLES

LIST OF SYMBOLS

β . . . . Shock Wave Angle

i . . . . Flow Relative Incidence Angle

$P_{reference}$ Transducer Reference Pressure

$P_{steady\text{-}state}$ . . . . . . Mean Static Pressure

$P(t)_{transient}$ High-Response Static Pressure

$P(\ )_{static}$ . . . . . . Overall Static Pressure

S . . . Estimated Transducer Sensitivity

θ . . . . Circumferential Position

U_{rotor} . . . . Rotor Tip Velocity

V_{axial} . . . . Axial Flow Velocity

$V_{relative}$ . . . . . . Relative Flow Velocity

$V(t)_{transient}$ . . Transducer Output Signal

1.0 INTRODUCTION

This report details the acquisition and reduction of Over-The-Rotor (OTR) static pressure data. These data were acquired during the Augmented Damping of Low Aspect Ratio Fans (ADLARF) test conducted at the Compressor Research Facility (CRF). The CRF is located at Wright Laboratory on Wright-Patterson A.F.B. in Ohio. The CRF is one of two high-speed compressor test facilities at Wright Laboratory and is described by Ostdiek et al. [1].

The report is primarily concerned with the acquisition and reduction of the OTR data, and is intended to demonstrate the ability to reduce, display, and analyze static pressure data acquired from the tip region of fans and compressors. The ability to show basic shock structure in the tip region of a transonic fan is clearly demonstrated. Problems associated with the acquisition and reduction process are also addressed. Although these data were originally intended only to demonstrate proof of concept, they have also provided valuable insight concerning the tip flow region of the ADLARF fan.

1.1 Rotor Tip Static Pressure Contours

The validation of state-of-the-art turbomachinery designs require comprehensive information concerning the flow behavior inside rotor blade passages. The ability to visualize tip flow structures in transonic compressors is an important step in the continuing effort to understand how these phenomena affect the overall performance. Static pressure measurements of the flow field inside blade passages successfully resolve flow phenomena such as tip leakage vortices and shock wave/boundary-layer interactions, both of which are believed to contribute to aerodynamic losses in transonic compressors and fans.

High-frequency response static pressure measurements have been successfully used to characterize intra-blade flow phenomena. Sellin et al. [2] used this method to identify tip flow structures in three different transonic designs. More recently, Copenhaver et al. [3] used similar data to characterize tip clearance effects in the flow field of a transonic rotor.

1

Determining the position of shock waves in front of and inside the blade passages of the first stage rotor was the motivation behind acquiring the rotor tip data presented in this report. Static pressure across a shock wave rises very nearly instantaneously, so it was hoped that this rapid change in pressure could be observed using high-frequency response pressure transducers. Not only were shock waves clearly resolved, but other flow phenomena, such as the previously mentioned tip leakage vortex, were observed in the OTR data. Indeed, the effort to acquire and reduce OTR data detailed in this report was entirely successful.

1.2 ADLARF Hardware

The ADLARF test article was a high-speed, two stage, low aspect ratio fan, shown schematically in Figure 1.1. In this report, all the data presented are from the first stage rotor. Table 1.1 shows the demonstrated baseline performance of the first stage rotor. For this machine, baseline performance for the entire compressor was achieved at 98.6% design speed; 100% design speed was 13,288 rpm. At the design point, the inlet relative Mach number was supersonic from approximately 75% blade span to the blade tip. During the OTR data acquisition portion of the test, a 16 blade solid rotor was used for the first stage. Some of the basic airfoil geometry parameters for this rotor are listed in Table 1.2.
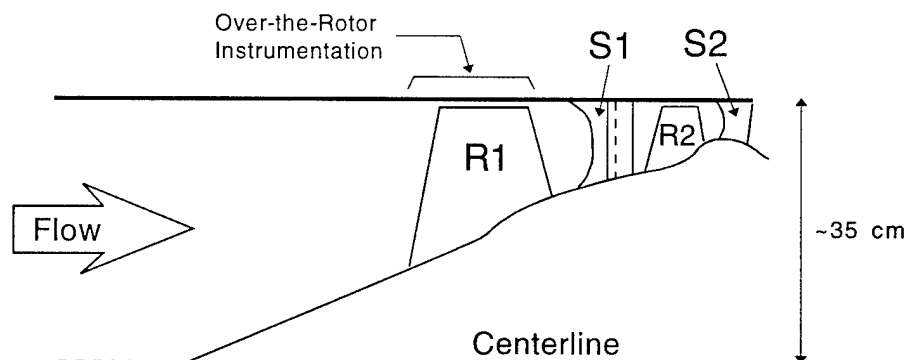
Figure 1.1   Meridional Schematic of ADLARF Compressor

2

Table 1.1 Rotor 1 Baseline Performance

Parameter	Value
Adiabatic Efficiency, Percent	88.9
Total Pressure Ratio	2.5
Total Temperature Ratio	1.3
Corrected Tip Speed, m/s	480.7 (1577 ft/sec)
Corrected Mass Flow, kg/sec	71.8 (158.3 lbm/sec)
Average Tip Clearance, mm	0.96 (0.038 in)
Tip Clearance/Actual Chord, %	0.46

Table 1.2 Airfoil Geometry Parameters for Rotor 1

Parameter	Value
Number of Blades	16
Average Aspect Ratio	1.22
Rotor Tip Radius, cm	35.24 (13.87 in)
Inlet Radius Ratio	0.33
Average Radius Ratio	0.47
Tip Solidity	1.50
Maximum Thickness/Tip Chord	0.028
Blade Tip Axial Chord, cm	11.43 (4.50 in)
Blade Tip Actual Chord, cm	20.79 (8.19 in)

2.0 DATA ACQUISITION AND REDUCTION

During the ADLARF test, transient and steady-state data were acquired with OTR instrumentation. In the context of this report, transient data refer to the high-response static pressure data, $P(t)_{transient}$, that were acquired in order to resolve the blade-to-blade variations in static pressure. Steady-state data refer to data that describe the average or mean static pressure, $P_{steady-state}$, at locations near the blade tip. The time dependent overall static pressure, $P(t)_{static}$, was determined by combining the transient and steady-state data in the following manner:

$$P(t)_{static} = P(t)_{transient} + P_{steady-state.}$$

The time dependent pressure was then ensemble averaged in an effort to reduce precision errors. The final result was an estimate of the circumferentially varying static pressure distribution, $P(\theta)_{static}$, near the rotor blade tip at 16 axial locations.

All the OTR data discussed in this report were acquired while the compressor was operating at 1 of 15 corrected, globally steady-state, operating points. No data were acquired during stalls, accels, decels, or geometry changes. The following subsections describe the OTR instrumentation and procedures used to acquire and reduce the data presented in this report.

2.1 Instrumentation and Data Acquisition

The $P(t)_{transient}$ data for this study were obtained using 16 high-frequency response pressure transducers mounted in an aluminum block that fit over the first stage rotor, shown schematically in Figure 2.1. The transducers were installed in a line parallel to the machine axis and were spaced 0.9525 cm (0.375 in; 8.3% of the axial chord) apart. The pressure ports and the pressure sensitive area of the transducers were both 0.097 cm (0.038 in) in diameter. The transducers were recessed 0.051 cm (0.2 in).

Installed along side the high-response transducers with the same spacing and axial positioning were 16 pressure ports for the $P_{steady-state}$ measurements. These measurements were obtained using the High Performance Data Acquisition System (HPDAS). HPDAS

4

is the principle performance data acquisition system used in the CRF. The heart of the HPDAS is a DEC 4000 model 90 work station, which controls the acquisition and reduction of the test data as well as monitors the health of the test compressor and the test facility.

Both sets of measurement ports are numbered from the leading edge to trailing edge, 1 to 16. Measurements obtained by the high-response transducers and the HPDAS are distinguished from one another by the nomenclature "PX#" and "PS#", respectively.
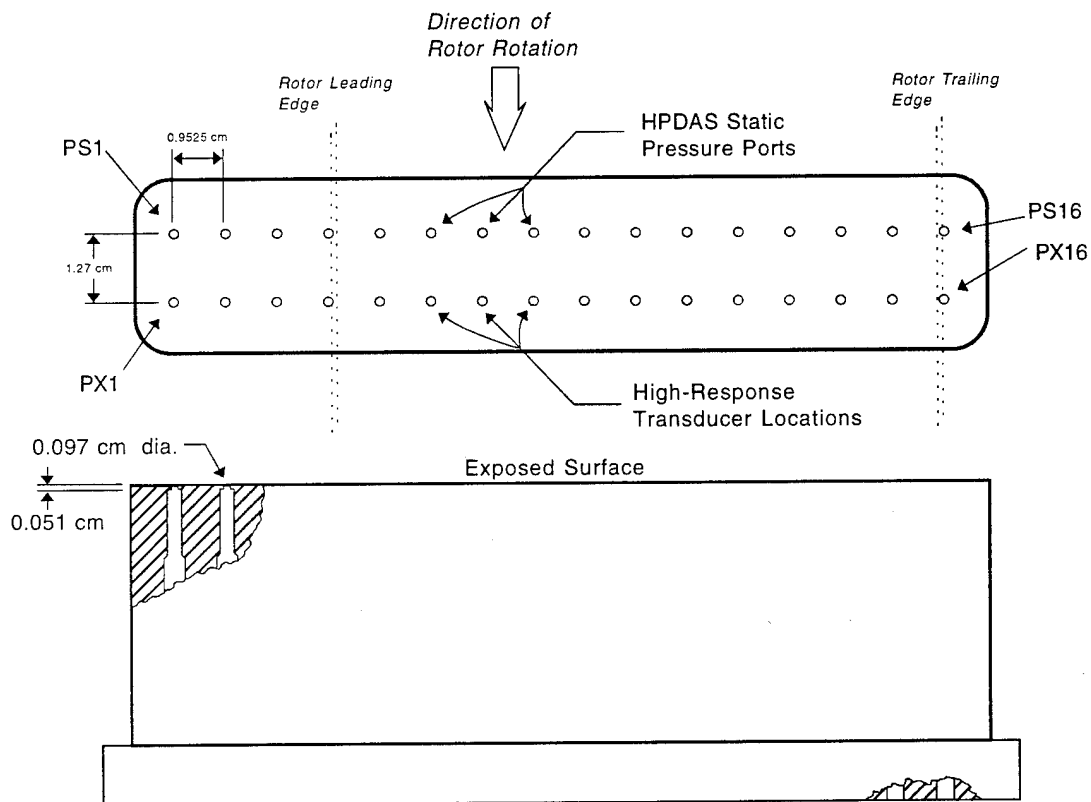
Figure 2.1 OTR Instrumentation Block

Eventual reduction of the transient pressure data required precise knowledge of the rotor speed. This was provided by a six-cycle-per-revolution, amplitude varying signal produced by a transducer arrangement located on and near the drive shaft.

Table 2.1 High-Response Transducer Information

Model	Kulite XCS-093
Differential Pressure Range	100 kPa (15 psid)
Operational Temperature Range	-55° C to 120°C (-65°F to 200°F)
Sensitivity	~ 2mV/kPa (~15mV/psi)
Temperature Sensitivity	±2% FS/35° C (100°F)
Excitation	15 V
Gain	50
Static Accuracy	±0.52 kPa (0.075 psi) or 0.5% FS
Coupling	AC or DC
Reference Pressure Measurement System	Heise PPG-149

2.1.1 Transient pressure measurements

As previously noted, transient static pressure data were acquired with the high-response transducers. Specific information concerning the high-response transducers is given in Table 2.1. The decision to use 100 kPa range transducers was based on an anticipated static pressure ratio of ~2 across the rotor. The chosen gain was sufficient to provide a maximum 5 V zero-to-peak signal to the analog tape recorder used to record the transducer signals for post-test processing. Signal processing hardware allowed the DC offset of the transducer signals to be retained or discarded as required. For the purposes of measuring the transient static pressure, $P(t)_{transient}$, the DC component was discarded.

The reference pressure, $P_{reference}$, for the high-response transducers was measured by a precise pressure measurement system with a static error of 0.15% of the measured pressure. The reference pressure used during data acquisition was usually 110 kPa. Different reference values were used during the calibration procedure, which is explained later in this section.

The transducer signals were recorded using a tape speed of 305 cps (120 ips).

6

This allowed signal frequencies of up to 80 kHz to be recorded without aliasing or distortion. To reduce phase shifting between channels during the post-test processing, an effort was made to record as much data as possible on one recorder head. The 28 channel tape recorder used has two recording heads, each recording 14 channels. There were 17 transducer channels, including the rotor speed signal, which meant that at least three channels had to be recorded using the other head. In actuality, 4 channels were recorded on one head and the remaining 13 on the other. During post-test processing, data from the 4 channels recorded on a different head were compared to the other 13 channels. No significant phase shifting was immediately evident, so no corrections were made to the data.

The maximum frequency response of the transducer alone was 150 kHz for a signal amplitude distortion ratio of < 1.01. Limitations associated with signal processing and recording procedures brought the frequency response of the system down to lower than 80 kHz. The measurement tube volume (0.051cm x 0.097cm dia.) further limited the frequency response to 38 kHz while maintaining the given maximum distortion ratio.

2.1.2 Steady-state pressure measurements

HPDAS data were acquired with Zero-Operate-Calibrate (ZOC) transducers. To minimize inaccuracies associated with temperature sensitivity, the ZOC transducers were mounted in a constant temperature cabinet. Several meters of nylon tubing connected the transducers to the measurement ports in the instrumentation block. This reduced the maximum frequency response of the HPDAS system to less than 200 Hz. The ZOC transducers were referenced to the atmospheric pressure at the time of the test. Measurements were therefore corrected by adding atmospheric pressure, as measured by a barometer, to the raw measurements. Steady-state data were obtained by calculating the average of 30 data scans taken over a period of 150 to 200 milliseconds. Once acquired, the HPDAS data were stored on digital tape and on computer printout. Specific information concerning the OTR/ HPDAS transducers is given in Table 2.2.

Table 2.2 HPDAS Transducer Information

Model	Scanivalve ZOC 14 (muxless)
Differential Pressure Range	345 kPa (50 psig)
Operational Temperature Range	5° C to 65°C (40°F to 150°F)
Sensitivity	~ 0.2mV/kPa (~1.5mV/psi)
Static Accuracy	±0.08% FS (worst case)
Excitation	5 V
Gain	50

2.1.3 Calibration procedure

Typically, bench calibrations are performed on high-response transducers before they are installed. This procedure verifies the linearity of the transducers and provides conversion coefficients (slope and offset) for eventual engineering unit conversion. However, because of the harsh operating environment of these transducers, an on-line calibration procedure was employed. This procedure took advantage of the fact that the high-response transducers measured differential pressure relative to a known reference value. This reference value could be changed during the test. Furthermore, the procedure also assumed that the mean pressure rise across the compressor was axisymmetric. In other words, the mean static pressure was assumed to be the same at PS1 and PX1, at PS2 and PX2, and so forth.

The first part of the on-line calibration procedure was to change the high-response transducer coupling from AC to DC. During the actual data acquisition portion of the test, the transducer signals are AC coupled; that is, the DC offset of the signal is removed before being recorded. For the purposes of calibration, the DC offset was retained while recording so that the transducer sensitivity (calibration slope) could be estimated for conversion of the transducer signals into engineering units.

While the system was DC coupled, the compressor was brought to some steady-state operating point and allowed to stabilize. Then the reference pressure to the transducers was changed to some known value, and the transducer output recorded for 1

minute. With the compressor remaining at the same steady-state operating point, this procedure was repeated using four or five different reference pressures. Although the compressor operating point remained unchanged throughout the entire procedure, the transducer measured different values of static pressure depending upon the reference pressures used. The actual steady-state static pressures at the rotor tip were obtained from the HPDAS steady-state data.

During post-processing, the HPDAS $P_{steady-state}$ data, the known $P_{reference}$ values, and the recorded high-response transducer signals were used to generate curve fits of measured static pressure as a function of mean output voltage for each transducer. The high-response transducer data provided the mean output voltage information while the difference between the actual static pressure and the known reference pressure, $P_{steady-state}$ - $P_{reference}$, provided the measured pressure for each data point on the calibration curve.

Mean output voltage was estimated by digitally processing the recorded high-response transducer output for each reference pressure change. Signal segments 2 seconds in length were digitally sampled at 100 samples per second for each transducer. The samples were then numerically averaged and the results were used as an estimate of the mean signal voltage. The standard deviations associated with each signal were calculated to provide some insight into the relative integrity of the estimated mean. No specific criteria were developed to determine whether or not a particular estimated mean was acceptable, but very large or very small values of standard deviation indicated problems with the recorded signal or the digitizing process.

Once the calibration data were processed, least-squares linear fits were calculated. These allowed estimates of slope, S, to be made for each high-response transducer. This entire calibration procedure was performed at least once each day during the OTR acquisition portion of the test. Therefore, to determine $P(t)_{transient}$ at each location, the estimated transducer sensitivity, S, for that particular test day and the high-response transducer AC signal, $V(t)_{transient}$, were multiplied. Mathematically, this is expressed as,

$$P(t)_{transient} = S(V(t)_{transient}).$$

2.2 Data Reduction

Following data acquisition, the OTR data were reduced and processed to create static pressure contour plots of the rotor tip region. This required digitizing and applying calibration information to the data, as well as ensemble-averaging to reduce precision error associated with signal noise. All of the final data were plotted and written to computer text files for storage and future processing.

2.2.1 Digitizing the high-response transducer data

In order to process the high-response data and eventually calculate $P(t)_{static}$, it was necessary to convert the analog recorded signals into digital form. This was done using the CRF in-house Analog Tape Digitizing System (ATDS). The basic configuration and operation of this system is described by Burns [4].

To determine the sample rate to use for the analog-to-digital conversion, it was necessary to estimate the highest possible frequency of interest in the data. In general, it is good practice to use the lowest sample rate possible, since high sample rates can quickly create very large data files. From the outset, frequencies 10 to 15 times greater that the blade passage frequency were thought to be the maximum possible frequency of interest. This was a purely arbitrary value, since it was unclear at this point exactly what the data would look like. As it turned out, this was more than adequate.

Experience has shown that 4 samples per cycle is best when resolving transient pressure data of this type [5]. Fewer samples per cycle are possible without any loss of frequency information, but the general character of the signal is then lost. If 4 samples per cycle are required, then the optimum sample rate will be approximately four times the maximum frequency of interest. Assuming a maximum frequency of interest 15 times greater than the blade passage frequency, the sample rate to use in this case was calculated to be 200 kHz (200,000 samples per second). This calculation is based on an assumed rotor frequency of 12,000 rpm (200 Hz) and sixteen rotor blades;

Sample Rate = (200 x 16 x 15 x 4) = 192,000 Hz or ~200,000 sps.

This sample rate was used at all rotor speeds, which meant that frequencies 15 to 18

times the blade passage frequency could be resolved depending upon the actual rotor speed.

Once the sample rate was determined, it was necessary to determine a low-pass analog filter frequency to prevent signal aliasing. The recorded high-response transducer signals were processed through this filter before being digitized. When choosing this frequency it was important to consider the Nyquist frequency criterion [5] and the frequency response characteristics of the low pass filter. To avoid signal aliasing, component frequencies greater than or equal to the Nyquist frequency, which is always half the sample rate, had to be filtered from the analog signal. The Nyquist frequency in this case was 100 kHz.

The analog, low-pass filter used was an eighth-order Butterworth filter. Because of the roll-off characteristics of this filter, component frequencies twice the cutoff frequency still maintained a measurable portion (0.4%) of their original amplitude. Therefore, to assure significant attenuation of the higher frequency components, the analog filter setting had to be no greater than half the Nyquist frequency, or one quarter of the sample rate. Thus, the maximum allowable filter setting in this case was 50 kHz.

It had already been determined that the highest frequency of interest would be no more than 15 times the blade passage frequency, or about 48 kHz. Since information concerning frequencies higher than 48 kHz was considered superfluous, this frequency became the limiting factor. A low-pass filter frequency of 48 kHz was therefore chosen, which was below the Nyquist frequency and the maximum analog filter setting allowed.

To avoid creating data files larger than necessary, the number of rotor revolutions required for further data processing was considered before the temporal length of each data set was chosen. For statistical reasons that are explained later in this section, at least 30 rotor revolutions of data were required. To provide a healthy error margin, approximately 100 revolutions per data set was chosen as a good working number. If the average rotor speed is once again considered to be 12,000 rpm (200 Hz), then approximately 0.5 sec of data is required for 100 revolutions. Therefore, all of the digitized data sets in this report are 0.5 sec (or 100,000 samples) in length, regardless of the rotor speed. As a result, the data sets in this report contain anywhere between 87 to

11

108 rotor revolutions of data, depending upon the rotor speed.

To digitize all 17 channels at 200,000 sps required an aggregate sample rate of 3.4 million sps, which was far greater than the maximum rate possible using the ATDS. It was therefore necessary to play the analog tape back at a slower speed than the original recording speed during the digitizing process. Using a record/playback speed ratio greater than one allowed the system to effectively sample at the required sample rate while using a much lower actual sample rate. A record/playback ratio of 16 was used to digitize the OTR data. The actual sample rate was then 12,500 sps, which required an aggregate rate of 212,500 sps. This was well within the limitations of the ATDS. This lower playback speed required changing some of the other digitizing parameters as well. The low-pass filter frequency was reduced to 3000 Hz while the temporal length became 8 sec. These changes maintained the effective filter and temporal length values of 48 kHz and 0.5 sec, respectively.

2.2.2 Ensemble averaging

To reduce precision errors associated with signal noise, $P(t)_{static}$ data were numerically ensemble-averaged. Data taken during each individual rotor revolution were treated as a single ensemble. Therefore, assuming a normal distribution, it was necessary to average the data over a minimum of 30 revolutions. Otherwise, the uncertainty associated with the estimated mean would have been unacceptable. As mentioned earlier, approximately 100 rotor revolutions were used. This value was well over the minimum requirement of 30 revolutions but was not such a large number that unacceptably large data files would be required. The required data file size became the real limiting factor, since the entire data reduction process required large amounts of data transfer between different computer systems.

The ensemble-averaging process used the rotor speed signal to provide precise knowledge of the rotor speed. This signal was a sixth rotor harmonic square-wave generated at the drive shaft. Using this signal, one rotor revolution was divided into six averaging windows (see Figure 2.2). The window size was dependent on the rotor speed, so the time length of each window varied during the averaging process. By allowing the

12
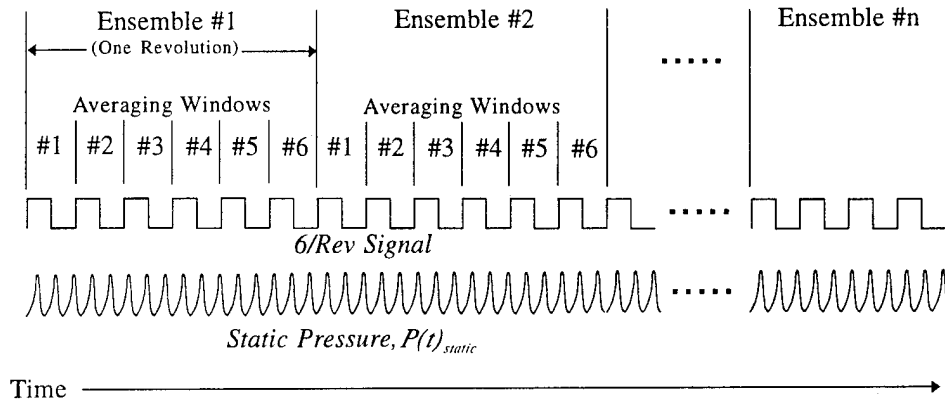
Figure 2.2 Ensemble-Averaging Window Sizing

window sizes to vary according to rotor speed, inaccuracies associated with temporal smearing of the data were minimized.

Each window was divided into 200 equally sized averaging bins. Ensemble-averaging was accomplished using the resulting 1200 averaging bins. The algorithm operated on all 16 transducer data sets simultaneously. In this way, a 1200 point, steady-state representation of the rotor tip static pressure variations during one revolution, $P(\theta)_{static}$, based on the ensemble average of approximately 100 revolutions, was produced for each measured compressor operating point at each of the 16 axial locations. The variable, θ, is the circumferential position.

2.2.3 Measurement uncertainty

A rudimentary uncertainty analysis was conducted on the OTR static pressure data system after the test. This analysis was based on the following assumptions:

1. The transducers (Kulites) were exposed to a maximum 82°C (180°F) temperature variation.

2. The frequency response of the applied pressures was no greater than 48 kHz.

13

A 3.03 kPa (0.44 psid, 0.88% FS) measurement uncertainty (95% confidence interval) was estimated for transducer measurements recorded on analog tape. The digitizing process brought the estimated uncertainty up to 3.17 kPa (0.46 psid, 0.92% FS). Assuming that the ensemble averaging process introduced a negligible bias error, the uncertainty in the presented data would be lower than 3.17 kPa, but it is unclear exactly how much lower.

3.0 OTR STATIC PRESSURE DATA

All of the OTR data presented in this report were acquired on the same test day. Two sets of calibration data (five points) were acquired near the middle of the day. Actual data were acquired at 5 different rotor speeds and at 3 different load conditions per speed for a total of 15 data points, as listed in Table 3.1. At each data point, transducer outputs were recorded on analog tape for 2 minutes. Hindsight has shown that 2 minutes of recorded data was unnecessary, since only the last 30 sec was considered for the analog-to-digital conversion, and only 0.5 sec of that 30 sec period was actually digitized.

Meanwhile, during the same 2 minute period, steady-state data were acquired through the HPDAS. These data, in conjunction with the calibration data, were used to convert the high-response transducer signals into engineering units per the digitizing and calibration procedures outlined earlier. In this way, fifteen 0.5 sec data files were created, each with 16 sets of pressure data and 1 set of rotor speed data organized in time increments of 0.05 μsec. Finally, the data files were ensemble-averaged and contour plotted using a convenient graphics software package. Unfortunately, the exact position of the blade tip relative to the magnet in the blisk used to produce the rotor speed signal was not known. Therefore the positioning of the rotor blade row relative to the flow field was estimated based on the pressure contours. The final ensemble-averaged data files were also converted to standard DOS text for storage purposes and future processing.

3.1 Performance

The measured values shown in Table 3.2 define the performance of rotor 1 during data acquisition. After comparing the information in Tables 3.1 and 3.2, it is clear that peak efficiency for the overall compressor is not necessarily peak efficiency for rotor 1. This is due to the proportionate higher loading of rotor 1 than rotor 2 at lower compressor speeds. At higher speeds, rotor 2 becomes more heavily loaded. Note that at 98.6% speed, the peak efficiency points for the overall compressor and for rotor 1 seem to agree.

15

Table 3.1 OTR Data Points

Data Point [*]	Percent Corrected Speed	Operating [@] Condition	Date & Time	CRF Analog Tape Number
1		Low Operating Line	272:18:08:11.0 - 11.5	1771
2	80%	Peak Efficiency	272:18:13:27.5 - 28.0	1772
3		Near Stall	272:20:06:10.5 - 11.0	1772
4		Low Operating Line	272:17:08:55.0 - 55.5	1759
5	85%	Peak Efficiency	272:17:06::06.0 -06.5	1759
6		Near Stall	272:16:50:29.0 - 29.5	1759
7		Low Operating Line	272:17:55:24.0 - 24.5	1771
8	90%	Peak Efficiency	272:17:58:30.0 - 30.5	1771
9		Near Stall	272:18:02:10.0 - 10.5	1771
10		Low Operating Line	272:17:38:30.0 - 30.5	1771
11	95%	Peak Efficiency	272:17:42:50.0 - 50.5	1771
12		Near Stall	272:17:48:49.0 - 49.5	1771
13		Low Operating Line	272:17:19:30.0 - 30.5	1771
14	98.6%	Peak Efficiency	272:17:25:50.0 - 50.5	1771
15		Near Stall	272:17:31:30.0 - 30.5	1771

* Data points were not acquired in this order, but are organized according to increasing speed and loading.

@ Note that the operating conditions (LOL, peak efficiency, near stall) are for the overall compressor and not for rotor 1 only.

Table 3.2 OTR Data Points; Rotor 1 Operating Conditions

Parameter	1	2	3	4	5	6	7	8	9	10	11	12	13	14	15
Cor. Rotor Speed, %	80			85			90			95			98.6		
Cor. Mass Flow, kg/s	54.9	53.7	51.4	61.1	60.4	56.4	66.4	66.0	62.2	71.3	70.9	67.0	73.2	73.0	69.9
Adiabatic Efficiency, %	88.0	86.9	84.2	90.1	89.5	85.7	91.3	91.0	87.8	91.3	91.2	88.4	88.6	88.9	87.4
Total Pressure Ratio	1.83	1.84	1.84	1.99	2.00	2.01	2.17	2.17	2.20	2.35	2.36	2.40	2.45	2.48	2.54
Total Temp. Ratio	1.21	1.22	1.23	1.24	1.24	1.26	1.27	1.27	1.29	1.30	1.30	1.32	1.33	1.33	1.35
Ave. Tip Clearance, mm	0.97	0.97	1.00	0.97	0.97	0.98	0.98	0.97	0.97	0.98	0.98	0.98	0.97	0.97	0.98
Tip Clearance to Actual Chord, %	0.47	0.47	0.48	0.47	0.47	0.47	0.47	0.47	0.47	0.47	0.47	0.47	0.47	0.47	0.47

Spanwise pressure ratio and efficiency profiles for 98.6% speed are shown in Figures 3.1 and 3.2, respectively. The pressure ratio plot shows that the outer 30 to 40% of the blade span is responsible for a significant portion of the average pressure rise across the rotor. The efficiency profile shows that this same region is responsible for a similarly large portion of the average rotor efficiency loss. Furthermore, most of the performance change from the lower operating line to near stall can be attributed to the tip region. Between the low operating line and near stall, the average rotor pressure ratio increased only 3.6% while the tip pressure ratio (90% span) increased 8.4%. Although not shown, similar trends are apparent from profile data acquired at the lower speeds. Clearly, the blade tip region plays a significant role in the overall performance of this rotor.

3.2 Static Pressure Contours

Figures 3.3 through 3.7 show contour plots produced using the static pressure data acquired over the blade tip. In these plots, air flow is from left to right and the blade rotation is from top to bottom. The three blade passages shown are representative of the 16 blade passages that comprise the entire rotor. A study of blade-to-blade variations was not the subject of this report, but to cursory review showed that there were no significant differences between the pressure fields in the sixteen blade passages. The same three blade passages are shown in all 15 contour plots. All the plots are identically scaled.

Shock wave geometry:

Shock waves are characterized by rapid increases in static pressure in the approximate direction of airflow (streamwise direction). Assuming this is true in the static data presented here, a single shock wave across the front portion of the rotor passage is evident at all 15 operating conditions. This passage shock wave runs from the pressure side of one blade near the leading edge to the suction side of the other blade, terminating somewhere near a point between 30 and 50% of the blade chord. It
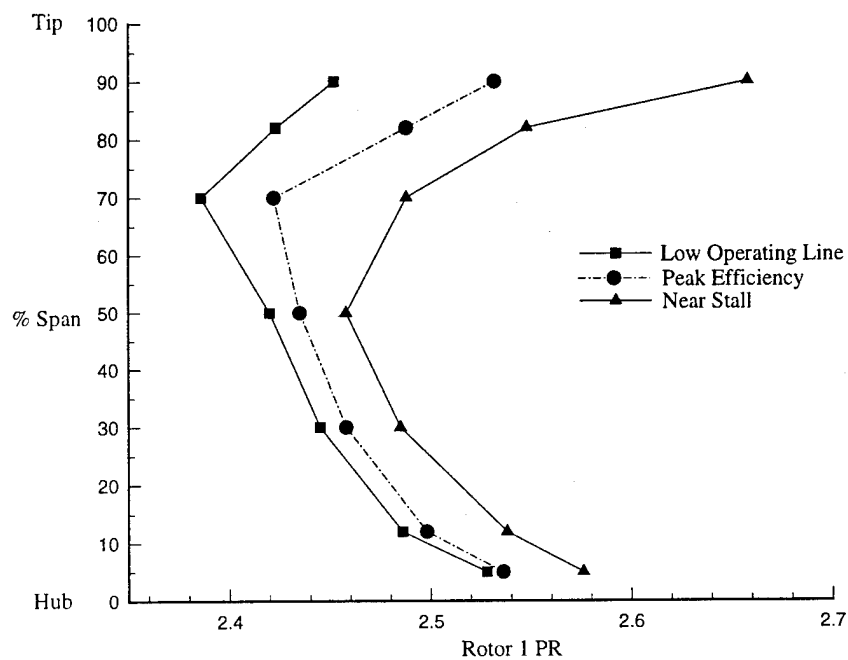
Figure 3.1 Spanwise Pressure Ratio Profiles for 98.6% Speed
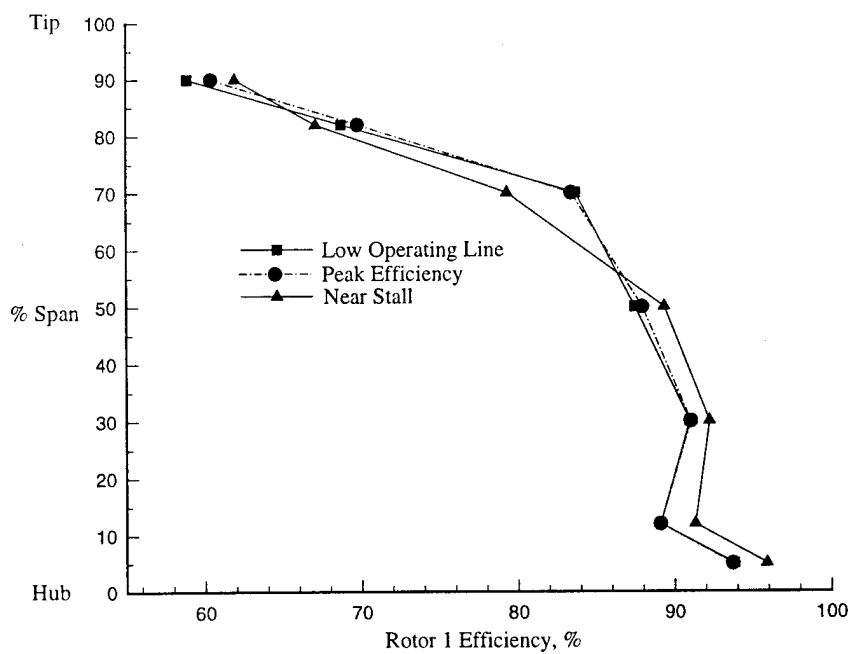
Figure 3.2 Spanwise Efficiency Profiles for 98.6% Speed

19
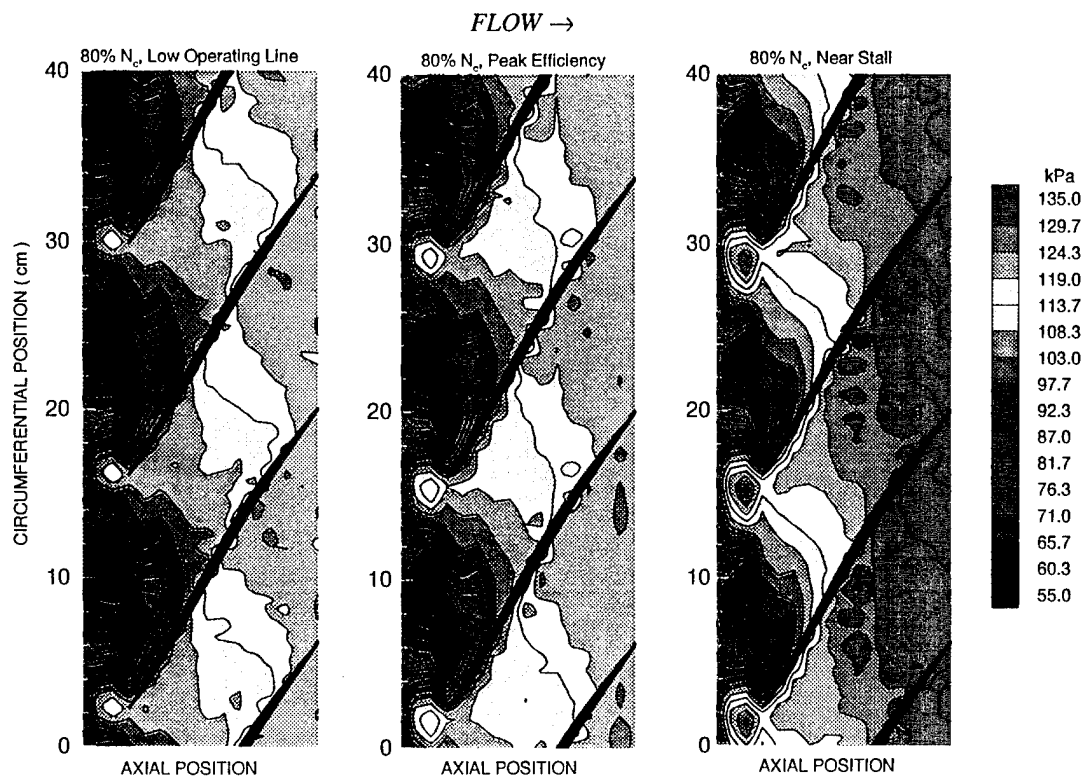
Figure 3.3   Rotor Tip Static Pressure Contours; 80% Design Speed

Figure 3.4   Rotor Tip Static Pressure Contours; 85% Design Speed

FLOW →

Figure 3.5   Rotor Tip Static Pressure Contours; 90% Design Speed

FLOW →

Figure 3.6   Rotor Tip Static Pressure Contours; 95% Design Speed

21

FLOW →

Figure 3.7   Rotor Tip Static Pressure Contours; 98% Design Speed

is noted that the pressure gradients across the shock waves in the data are not as sharp as expected. This is presumably caused by shock turbulence, data smoothing resulting from the ensemble averaging process, and interaction with other flow structures in the blade passage.
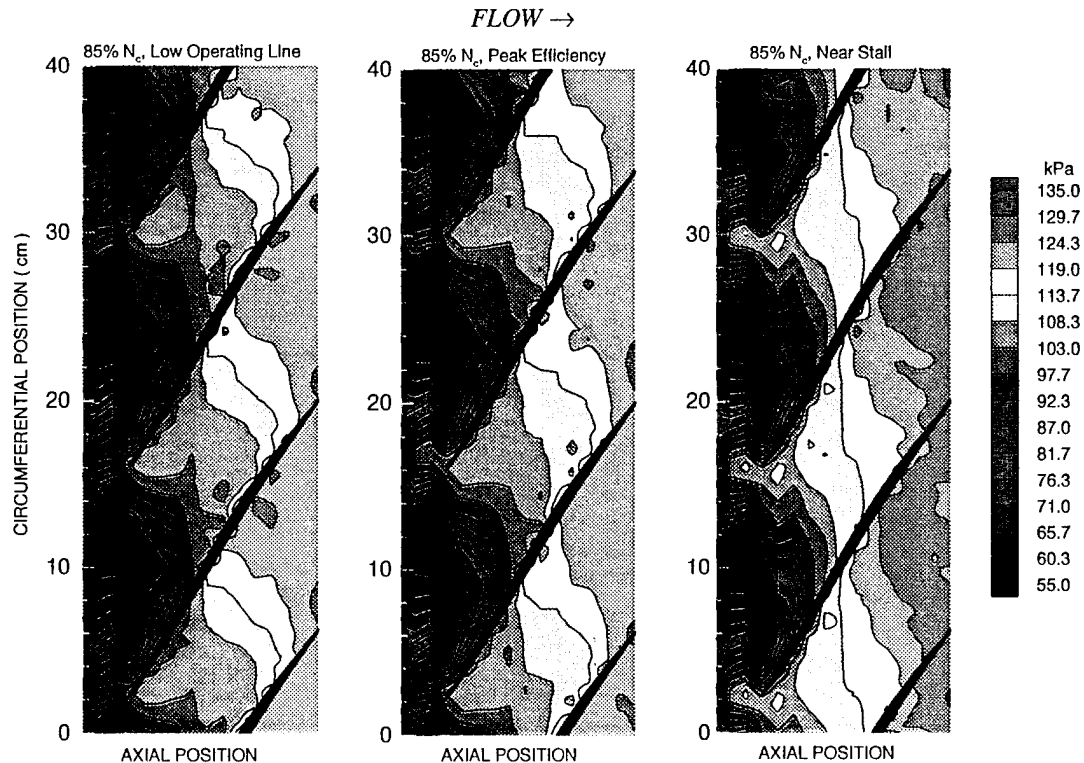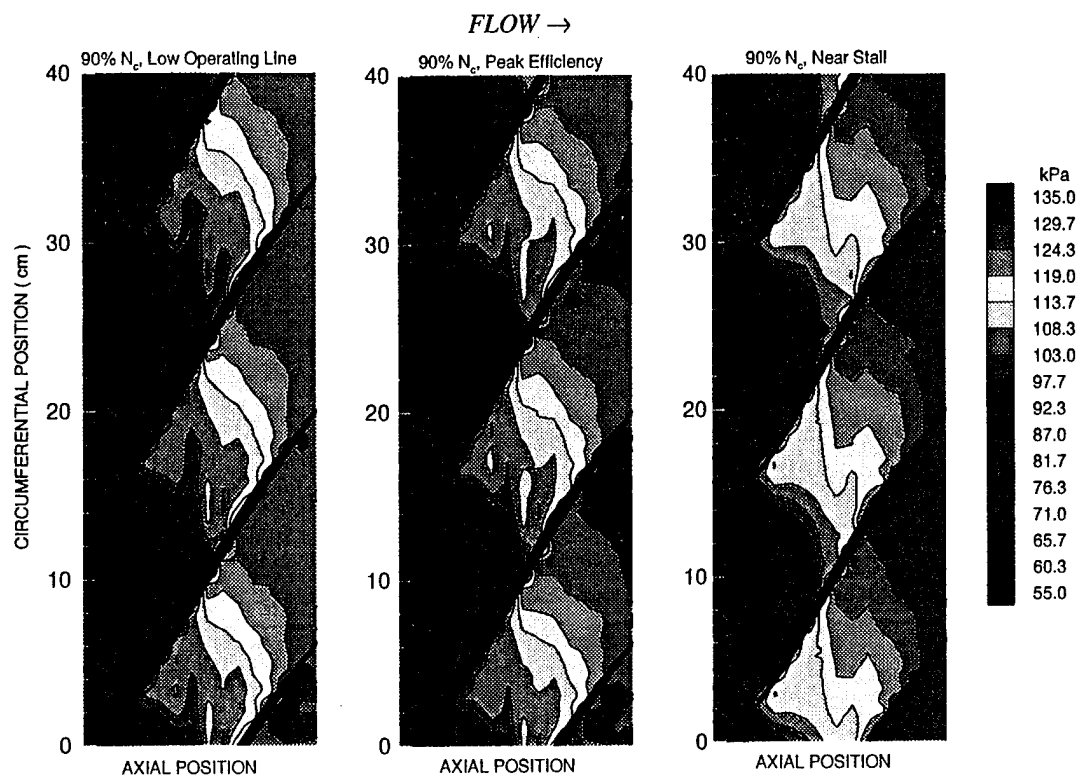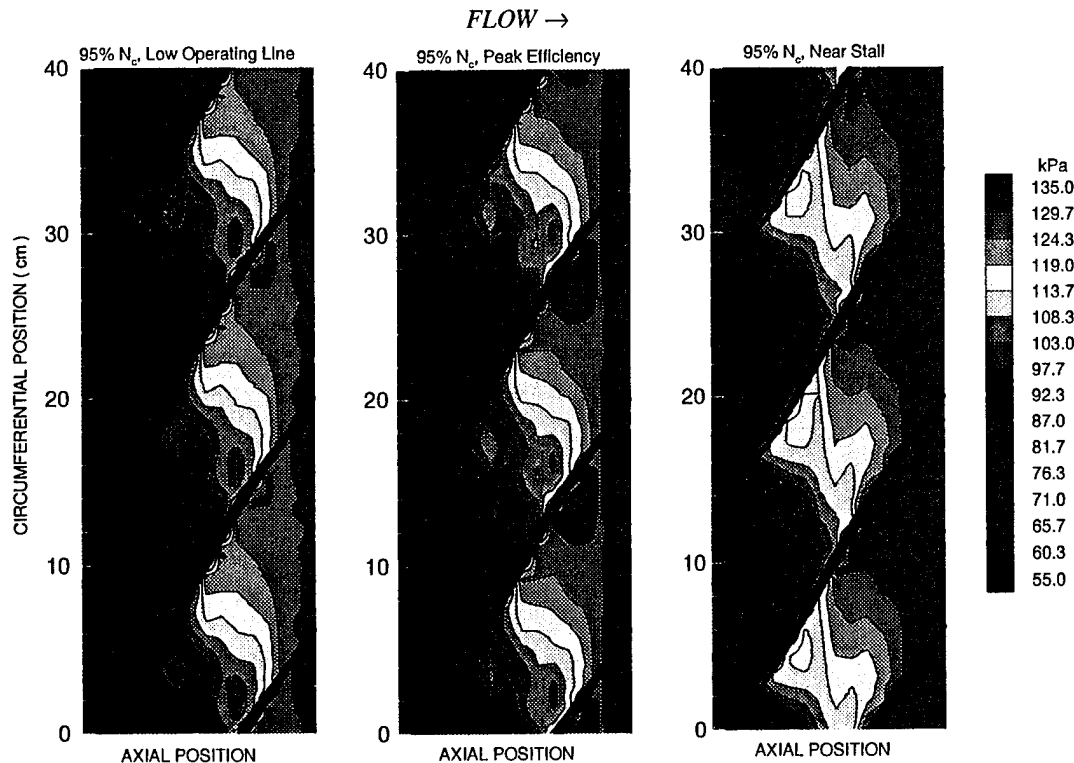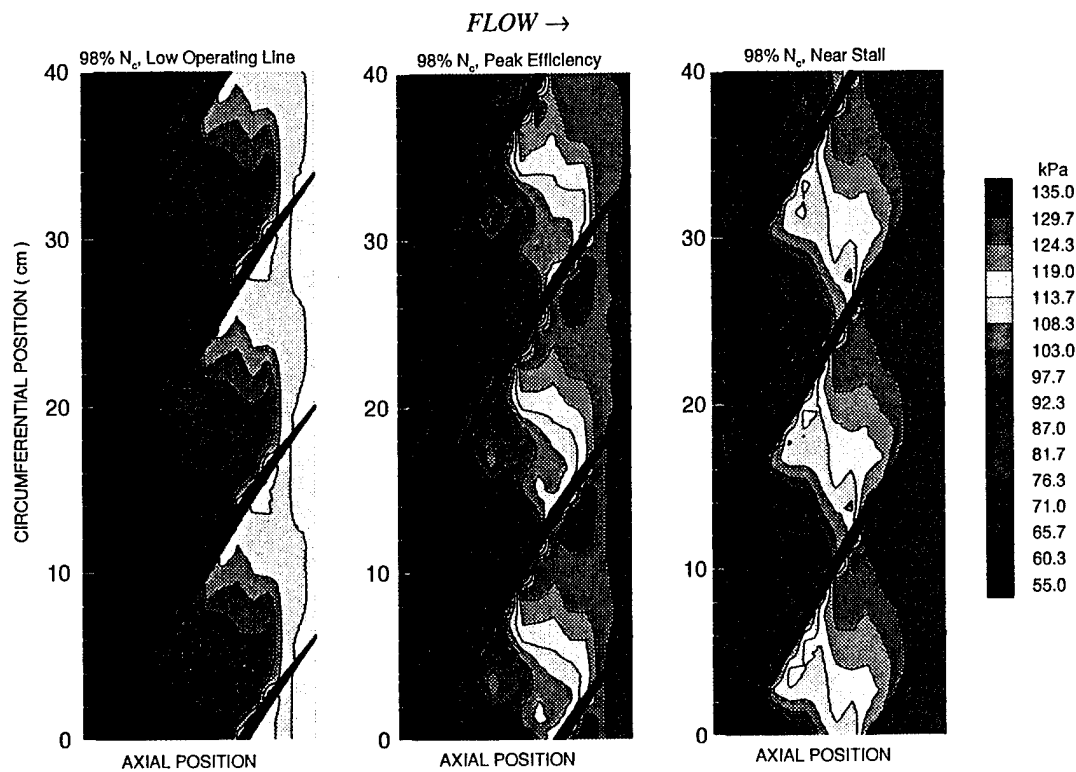
The exact angle of the shock wave relative to the blade varies as a function compressor loading. As the compressor is loaded, the axial velocity, V_{axial}, decreases as a result of decreasing mass flow, and if the rotor tip velocity, U_{rotor}, remains constant, then the relative flow velocity, $V_{relative}$, decreases. This increases the flow relative incidence angle, i , and consequently, alters the relative flow direction at the blade leading edge, as shown in Figure 3.8. Since the shock wave angle, β, is directly related to the flow relative incidence angle, any change in incidence will alter the shock geometry. Thus, the shock wave angle tends to increase as the compressor operating point moves from the low operating line to near stall, as Figure 3.8 shows.

At all five speeds, the geometry of the shock wave in the OTR data changes as compressor loading is varied. At 80% speed, the shock wave is detached, forming a bow shock just upstream from the leading edge. It remains detached at all three operating conditions. The bow shock increases in relative strength as loading is increased. This is evident from the high pressure zone upstream of the leading edge but just downstream of the shock. The static pressure in this zone increases significantly as the compressor becomes more highly loaded. The shock angle does not seem to change much as the compressor is loaded, but the shock wave appears to move upstream as the compressor operating point moves from the low operating line to near stall.

The 85% speed data indicate shock wave behavior similar to that observed in the 80% speed data, but it is unclear in this case whether or not the shock wave is fully detached from the leading edge. At near stall, it is likely that the shock wave is detached. However, at the two other operating conditions, the data can be interpreted in two ways. The high pressure zone upstream, and slightly offset circumferentially, from the leading edge could be the static pressure rise resulting from a bow shock.This flow structure could also result from a set of pre-compression and expansion waves near the leading edge.
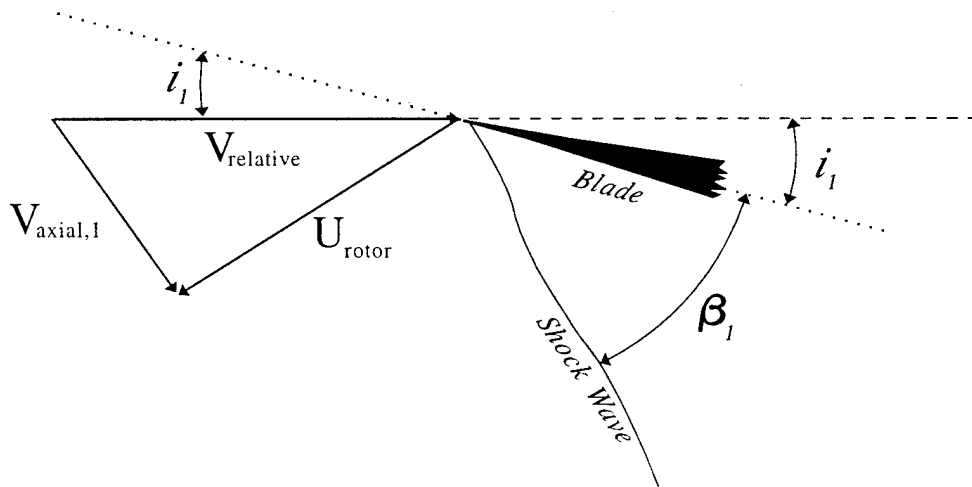
Low Operating Line

High Axial Velocity, V_{axial}; Low Relative Incidence Angle, i_1
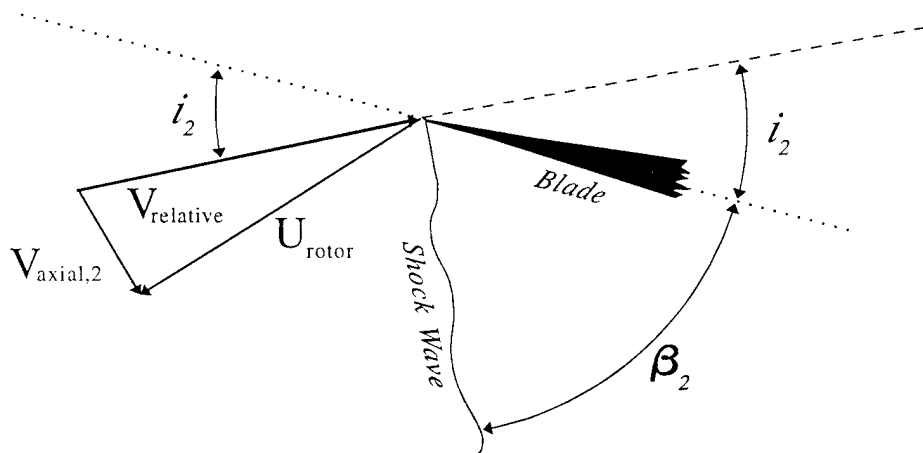
Near Stall

Low Axial Velocity, V_{axial}; High Relative Incidence Angle, i_1

$$\beta_1 < \beta_2$$

Figure 3.8 Effect of Incident Angle on Shock Wave Angle

A precompression wave is distinguished from a shock wave by a smaller (though still considerable) increase in static pressure in the steamwise direction across the wave. Expansion waves are characterized by a corresponding decrease in static pressure in the streamwise direction. If interpreted this way, the data show precompression waves just upstream of the leading edge. Expansion waves are evident downstream from the precompression waves and seem to be attached to the suction surface of the blade just downstream of the leading edge. The existence and position of these waves agrees well with laser anemometer data obtained in a previous test of this compressor and presented by Rabe [6]. Rabe theorized that these phenomena are the result of the concave shape of the suction surface just behind the leading edge, which is part of the S-shaped nature of the blade. It can be argued that these waves exist whether or not the passage shock wave is detached. Indeed, evidence suggesting the existence of precompression and expansion waves exists in the presented data at all 5 speeds.

The data from 90%, 95%, and 98.6% speeds indicate that one end of the passage shock wave remains attached to the pressure side blade leading edge for all operating conditions. Furthermore, the passage shock wave becomes more normal to the flow as compressor loading is increased. In the data, one end of the shock wave appears to remain fixed to the pressure side while the other end moves upstream as the compressor is loaded. In this way, the shock wave appears to pivot about the blade leading edge.

To provide some confidence in the static pressure data, the measured shock wave angle was compared to the calculated angle at 98.6% speed, peak efficiency. It was not possible to obtain an exact measurement of the angle from static pressure data because of the diffuse nature of the pressure gradient, but it was possible to specify a reasonable range of angles. Thus, the shock wave angle was estimated to be somewhere between 83 and 85°.

Laser anemometry (LA) data obtained from the tip leading edge of the compressor earlier in the test program was used to help calculate the shock angle. The average relative Mach number and flow angle measured by the LA system at the tip leading edge were 1.8 and 62.5°, respectively. The blade angle at the tip leading edge is 54°. The difference between the flow and blade angles, 8.5°, was the flow relative incidence angle.

25

Using the relative Mach number and flow relative incidence angle, the shock wave angle was calculated using basic oblique shock relations [7]. The calculated shock wave angle was 83.5°, which compares rather well with the measured angle considering the measurement methods.

Tip leakage vortices:

Evidence of leakage vortices is also observed in the data. Shown schematically in Figure 3.9, a tip leakage vortex occurs where the air flow interacts with both the blade tip and the case wall. Sellin et al. [2] saw significant pressure disturbances on the suction side of the blades in the transonic compressor rotors they tested, which they interpreted as evidence of tip leakage vortices. In the data presented in this report, the existence of similar leakage vortices can also be inferred. All 15 data sets show a bending of the
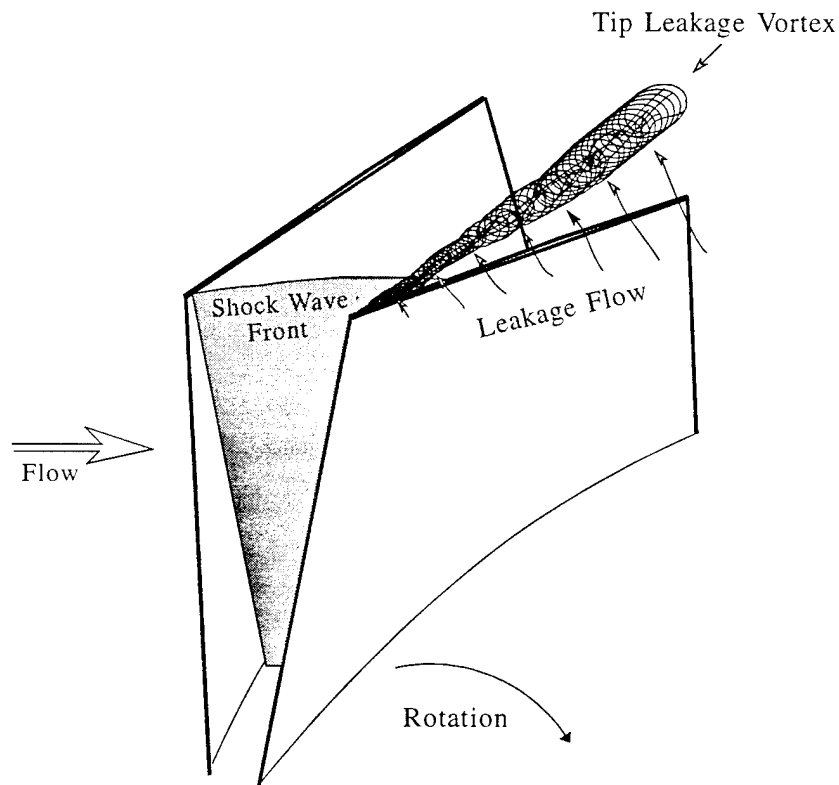

Figure 3.9 Schematic Representation of a Tip Leakage Vortex

pressure contours near the suction side of the blade passage just in front of the shock wave. Small "bumps" or curves in the contours downstream of the shock wave, starting near the suction surface, are also present in some of the data.

For example, at 90% speed (Figure 3.5), near stall, the pressure contours upstream of the shock wave seem to bend from the middle of the blade passage towards the suction surface. Small curves in the pressure contours are present from behind the shock wave downstream to about 60% axial chord. This pressure disturbance seems to move diagonally across the blade passage from the suction surface to near the pressure surface of the adjacent blade. The bending and small curves in the pressure contours are the static pressure "footprint" of the tip leakage vortex. The bending of the contours upstream of the shock wave is a result of interaction between the shock wave and the leakage vortex. The small curves in the contours are static pressure disturbances caused by the vortex itself.

The vortex induced curvatures in the pressure contour data change when the compressor operating point is varied. It appears that the extent of the vortex increases as the compressor operating point moves from the low operating line to near stall. At the same time, the degree of interaction between the vortex and the shock wave seems to decrease. This behavior is best observed at 95% speed (Figure 3.6). At the low operating line there is a low static pressure zone near the suction side of the passage just behind the shock wave. This suggests a local weakening of the shock wave due to some flow disturbance, such as a leakage vortex. Downstream from the shock wave, there are slight contour curvatures suggesting a vortex (as previously discussed), but they do not progress very far down or across the passage (about 50% axial chord). At peak efficiency, the low pressure zone becomes smaller while the contour curvatures just downstream become slightly more pronounced, extending down the blade passage to approximately the same point as before. Finally, at near stall, the low pressure zone disappears altogether, but the vortex now appears to extend much farther downstream (about 70% axial chord) and stretches across to the pressure side of the blade passage.

These observations suggest that the shock wave loses strength as the compressor becomes more highly loaded, thus allowing the tip leakage vortex remain intact as it

traverses the shock wave. This agrees well with oblique shock theory, which predicts a decrease in shock strength (less difference between the upstream and downstream Mach number) with increasing incidence angle. All of this seems to validate the design of the rotor, since the goal of most transonic designs is to reduce the shock strength, and therefore the losses due to entropy, at the higher load conditions.

Problems:

These data provided useful information concerning the intra-blade flow field near the tip of this transonic rotor. However, several deficiencies and errors were observed after reviewing the data.

1)   At least two of the transducers used to measure steady-state pressure produced consistently low measurement values. The effect this had on the data is especially apparent at 90% speed (Figure 3.5). The measurements at the blade leading edge and at about 25% chord are too low, which introduced a bias that is obvious in the data. This problem is evident in all of the contour data to varying degrees.

2)   Two of the high-response transducers seemed to function intermittently. This resulted in lines running through the contour data in the circumferential direction. These are evident near the trailing edge at 95 and 98.6% speed (Figures 3.6 and 3.7) and near 60% chord at 80 and 85% speed (Figures 3.3 and 3.4). Both transducers seemed to function fine at 90% speed (Figure 3.5).

3)   The correct positioning of the rotor blades relative to the data also posed a significant problem that was never precisely solved. An attempt was made to position the blades using the rotor speed signal, but blade deflection and untwist at different rotor speeds and operating conditions could not be properly compensated for, so the position of the leading edge could not be verified. In all of the contour plots the blades are positioned by eye and therefore may or may not be exact.

4.0 CONCLUSIONS

The following conclusions can be made concerning the intra-blade static pressure field in the tip region of the test rotor used in this study:

- The passage shock wave geometry changes as the speed and loading is varied. At lower speeds (80%), the shock wave is detached from the blade leading edge at least part of time. At higher speeds (greater than 80%) , the shock wave is attached to the leading edge. Furthermore, the behavior of the attached shock wave agrees well with oblique shock theory.

- Tip leakage vortices are present in this rotor. The axial and circumferential extent of these vortices increase as the compressor loading is increased. The vortices are significantly weakened or destroyed by the passage shock waves at the low operating line and peak efficiency, but appear to be less affected by the shocks at near stall. This implies that the passage shock wave grows weaker as the operating point moves from the low operating line to near stall.

Based on the work conducted to complete this report, it is concluded that the methods outlined in this report are satisfactory for the acquisition, reduction, and resolution of rotor tip static pressure data. Although certain aspects need refinement, the basic procedure is sound.

5.0 RECOMMENDATIONS

Based upon the observations of this author and other researchers, the following recommendations are made regarding any future acquisition of rotor tip static pressure data in the CRF:

1. Calibration procedures should be developed and followed that allow more frequent recalculation of the high-response transducer sensitivities. Because data were often recorded on different tapes and at different times, significant differences between signals from the same transducer were often observed during playback. If at least one set of calibration data had been available on each tape, these differences would have been easier to correct. Unfortunately, during the data reduction phase of this report, only two sets of calibration data were available for all of the data recorded, and these were on the same tape.

2. A better method of determining blade position relative to the transducers needs to be determined. Although it was theoretically possible to do this with the ADLARF data, necessary measurements and deformation predictions were not made before the test. During future CRF compressor tests of which this author is aware, determining blade position will become even more problematic.

3. Ways of speeding up the reduction and processing time need to be explored. The time required to produce just 1 of the 15 contour plots in this report was nearly 2 hours (this includes the digitizing the data to the final printing of the contour plot). Methods are already under development which will cut this time down to under 1 hour, but this too can be improved.

4. The benefits of reducing the tip static pressure data during the test in near real-time need to be explored. This would reduce errors associated with the recording/playback system.

REFERENCES

1.   Ostdiek, F. R., Copenhaver, W. W., and Rabe, D. C., 1989, "Compressor Performance Tests in the Compressor Research Facility," AGARD Conference on Unsteady Aerodynamic Phenomena in Turbomachines, Proceedings No. 486.

2.   Sellin, M. D., Puterbaugh, S. L., and Copenhaver, W. W., 1993, "Tip Shock Structures in Transonic Compressor Rotors," AIAA 93-1869, 29th Joint Propulsion Conference and Exhibit, Monteray, CA..

3.   Copenhaver, W. W., Mayhew, E. R., and Hah C., "The Effect of Tip Clearance on a Swept Transonic Compressor Rotor," ASME Paper 94-GT-363

4.   Burns, M. B., Post-processing Function/Analog Tape Digitizing System (ATDS), ATDS User's Guide, CRF Operation Manual, 28 May 1992 Revision (Unpublished).

5.   Bendat, J. S., and Piersol, A. G., Random Data, Analysis and Measurement Procedures, 2nd Edition, 1986, John Wiley & Sons, New York.

6.   Rabe, D. C., Wennerstrom, A. J., and O'Brien, W. F., "Characterization of Shock Wave End Wall Boundary Layer Interactions in a Transonic Compressor," ASME *Journal of Turbomachinery*, Vol. 110, No. 3, July 1988, pp. 386-392.

7.   Ames Research Staff, *Equations, Tables, and Charts for Compressible Flow*, NACA Report 1135

APPENDIX: Current CRF Tip Static Pressure Measurement Efforts

The tip static pressure measurement techniques used to produce the data presented in this report have since been substantially enhanced. The CRF currently uses an on-line acquisition and reduction system that produces similar graphic data in near real-time. Furthermore, on-line calibration procedures have been developed that allow more frequent recalculation of the high-response transducer sensitivities.

The heart of acquisition and reduction system is a Masscomp (MC6400) computer using a 32 channel, 1.6 MHz analog-to-digital converter with sample and hold capability. Software was written for this computer that acquires and reduces the high-response transducer data. The processed data are then transferred over a network to a 486 PC to produce the contour plots. The time between data acquisition and the final printing of the contour plots is approximately 10 minutes using this system.

Transducer calibration is accomplished using the Masscomp and the HPDAS. On-line data acquisition and reduction software written for the HPDAS was modified so that steady-state pressure measurements could be automatically transferred to the Masscomp. Control software that runs in parallel with the HPDAS was modified to allow on-line variation of the high-response transducer reference pressures. Both of these modifications greatly improved the degree of automation in the calibration process and significantly reduced the time and effort needed to accomplish on-line calibration of the high-response transducers.

The improved tip static pressure measurement system was successfully used during a recent compressor test. Feedback from other researchers involved in this test has all been positive. None the less, further improvements are planned.